

A Dataset of Laryngeal Endoscopic Images with Comparative Study on Convolution Neural Network Based Semantic Segmentation

Max-Heinrich Laves · Jens Bicker · Lüder
A. Kahrs · Tobias Ortmaier

Received: date / Accepted: date

Abstract *Purpose* Automated segmentation of anatomical structures in medical image analysis is a key step in defining topology to enable or assist autonomous intervention robots. Recent methods based on deep convolutional neural networks (CNN) have outperformed former heuristic methods. However, those methods were primarily evaluated on rigid, real-world environments. In this study, we evaluate existing segmentation methods for their use with soft tissue.

Methods The four CNN-based methods SegNet, UNet, ENet and ErfNet are trained with high supervision on a novel 7-class dataset of surgeries on the human larynx. The dataset contains 400 manually segmented images from two patients during laser incisions. The Intersection-over-Union (IoU) evaluation metric is used to measure the accuracy of each method. Stochastic inference is used to show the uncertainty of the individual models.

Results Our study shows that ErfNet is best suited for laryngeal soft tissue with a mean IoU of 48.6 %. The highest efficiency is achieved by ENet with a mean inference time of 9.22 ms per image on an NVIDIA GeForce GTX 1080 Ti GPGPU.

Conclusion CNN-based methods for semantic segmentation are applicable to laryngeal soft tissue. The segmentation can be used for active constraints or autonomous control in robot-assisted laser surgery. Further improvements could be achieved by using a larger dataset or training the models in a self-supervised manner.

Keywords Computer Vision · Larynx · Vocal folds · Soft tissue · Open access dataset · Machine learning

Max-Heinrich Laves · Jens Bicker · Lüder A. Kahrs · Tobias Ortmaier
Appelstraße 11A
30167 Hannover, Germany
Tel.: +49 511 762 19617
Fax: +49 511 762 19976
E-mail: laves@imes.uni-hannover.de

1 Introduction

Diagnosis of pathologies using laryngeal endoscopic images may make early detection possible [5]. Vocal folds, as the main functional organ within the larynx, are sensitive structures for surgery. Computer vision has the potential to assist the physician in restoring or preserving the voice. This can be achieved by combining augmented reality [27], robotics [9] and laser surgery [26] with image processing methods. Segmentation of laryngeal images is one of the most important components for successful operation of such a system.

1.1 Outline

This paper discusses the segmentation of laryngeal soft tissue as a prerequisite for robot-assisted laser incisions. Therefore, we investigate state-of-the-art segmentation methods, all based on deep convolutional neural networks, and compare them on a novel manually annotated in vivo dataset of human vocal folds. Subsequent to the description of the implementation differences of the selected models, we define our test setup and present the results. The article concludes with a discussion of the limitations of the approaches chosen and gives an outlook on possible improvements.

1.2 Related Work

Image segmentation is the task of partitioning an image into several non-intersecting *coherent* parts and is an important step of early vision [18]. In laryngeal scenes, segmentation on high-speed or stroboscopic videos is done to automatically extract the contours of the vocal folds to analyze the fold vibrations [1] and the glottal space to characterize glottal closure and other vocal fold pathologies [17]. The ultimate goal in medical image segmentation is recognizing real-world objects in image data fully automatically, with high accuracy and efficiency. However, early methods were not capable of doing this and demanded a human supervisor to initialize a method, check the result, or even to correct the segmentation afterwards [16]. These techniques are based on manually selected low-level image characteristics such as grayscale thresholds, pixel color, edge detection or region growing [8, 17, 22] and are therefore strongly affected by image noise or illumination changes [18]. Additionally, these procedures do not perform a semantic assumption of the segmented areas.

More sophisticated methods are based on mathematical models and rely on finding the parameters with which the output of the model minimizes an error or energy function. Some of these approaches require ground truth examples prior to or during the segmentation task. In atlas-based segmentation, for example, a manually segmented “atlas”, which acts as a-priori anatomical information, is matched onto the input image [6]. This turns the segmentation problem to a registration problem. The error-minimizing transformation between the images is also applied to the a-priori segmentation, which results in the segmentation of the input image. A good result requires a large atlas database, which must be

considered during segmentation time, thus making atlas-based segmentation not applicable in environments with real-time demands.

Artificial neural networks (ANN) have been used in medical image segmentation for a long time and are characterized by their robustness to image noise and real-time capable output due to their massively parallel structure [6, 15, 17, 18, 23]. The performance of early ANNs with low numbers of neural layers were not superior compared to other methods. However, due to the recent progress in the field of convolutional neural networks, new segmentation methods with outstanding performance have been created. On image classification tasks, CNN-based approaches already exceed human-level performance [12]. Long et al. first proposed a fully convolutional network (FCN) which was trained pixel-to-pixel and exceeded the former state-of-the-art by up to 20 % on the PASCAL VOC 2012 dataset [14]. This led to the emergence of many new CNN-based segmentation methods. In the following, we will focus on potential real-time capable network architectures, as the segmentation result will be used later for intra-operative robot and laser control. Therefore, we will subsequently discuss four selected methods, which already showed promising results on other datasets.

One focus of this research includes the automatic detection of pathological and non-pathological areas. Researchers have developed algorithms for the classification of laryngeal tumors based on narrow band imaging (NBI) and surrounding blood vessel structures [4]. Others have used classifications based on a combination of the vocal fold shape and vascular pattern [31]. It has also been attempted to correlate voice pathologies with endoscopic videos of the vocal fold [19]. Furthermore, high-speed videos are analyzed with wavelet-based phonovibrograms and it is shown that a distinction between malignant and precancerous vocal fold lesions is possible [32]. Recently, automatic detection of vocal fold tumor tissue has been performed with confocal laser endomicroscopy and convolutional neural networks [2]. Nevertheless, we see a lack of publicly available datasets of laryngeal (vocal fold) micro- and endoscopic images associated with segmentation.

2 Materials and Methods

First of all we will present our dataset of segmented vocal fold images. The machine learning methods used in this study are then briefly described and compared with each other in terms of their implementation. At the end of this section, the evaluation environment is defined.

2.1 The Vocal Folds Dataset

All subsequently described models are trained and evaluated on a dataset, containing 400 manually segmented in vivo color images of the larynx during two different resection surgeries with a resolution of 512×512 pixels. The images have been captured with a stereo endoscope (VSii, Visionsense, Petach-Tikva, Israel) in an in vivo laryngeal surgery and have been used in prior studies [28]. They are categorized in the 7 different classes *void*, *vocal folds*, *other tissue*, *glottal space*, *pathology*, *surgical tool* and *intubation* with indices $\{0, 1, 2, 3, 4, 5, 6\}$, respectively, which is represented by the gray values of the label maps. The dataset consists of

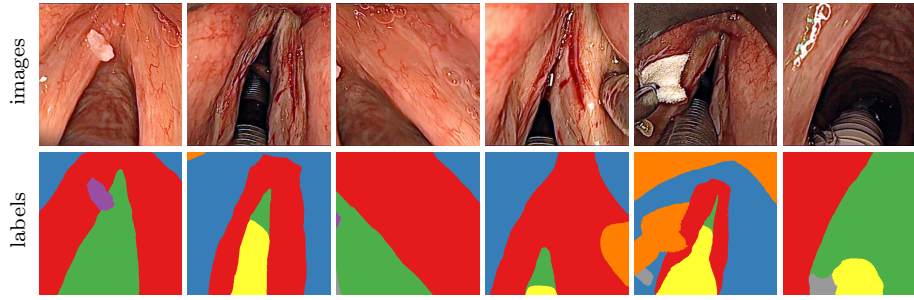


Fig. 1 First row: Examples from vocal folds dataset. Second row: Manually segmented ground truth label maps with classes *vocal folds* (red), *other tissue* (blue), *glottal space* (green), *pathology* (purple), *surgical tool* (orange), *intubation* (yellow) and *void* (grey). The grayscale label maps have been colorized for better visualization.

5 different sequences from two patients (named SEQ1–SEQ3 from patient 1 and SEQ7 and SEQ8 from patient 2). The sequences have following characteristics (see Fig. 1):

- SEQ1: pre-operative with clearly visible tumor on vocal fold, changes in translation, rotation, scale, no instruments visible, without intubation
- SEQ2: pre-operative with clearly visible tumor, visible instruments, changes in translation and scale, with intubation
- SEQ3: post-operative with removed tumor, damaged tissue, changes in translation and scale, with intubation
- SEQ7: pre-operative with instruments manipulating and grasping the vocal folds, changes in translation and scale, with intubation
- SEQ8: post-operative with blood on vocal folds, instruments and surgical dressing, with intubation

Subsequent images have a temporal contiguity as they are sampled uniformly from videos. In order to reduce inter-frame correlation, images were extracted from the original videos only once per second. Segmentations have been manually created on a pen display (DTK-2241, K. K. Wacom). Figure 2 shows the distribution of the annotated pixels per class. The dataset is publicly available¹ and will be extended in the future.

2.2 UNet

UNet is a fully convolutional U-shaped network architecture for biomedical image segmentation [25]. The first part is inspired by FCN [14] and acts as an encoder. It consists of repeated 3×3 convolutions. The feature maps are saved for later use before downsampling with 2×2 max-pooling. The number of feature maps are doubled after each downsampling. Dropout is applied at the end of the encoder. To generate a dense segmentation output, unlike simple upsampling in FCN, the encoder is inverted, and pooling is replaced by transposed convolution (up-conv). This acts as a decoder and creates a nearly symmetrical encoder-decoder network.

¹ <https://github.com/imesluh/vocalfolds>

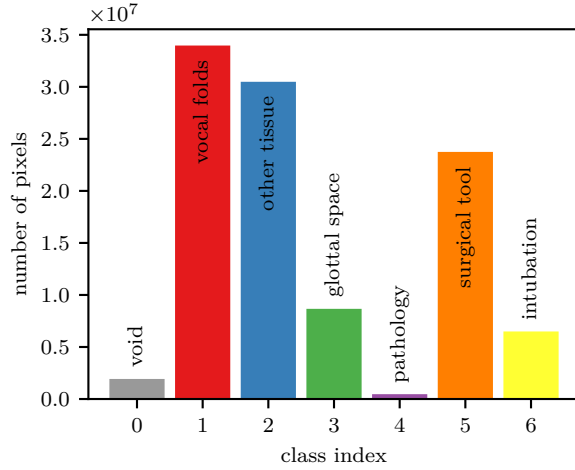


Fig. 2 Number of annotated pixels per class in the dataset.

Name	Type	Output Size
input	RGB image	$3 \times 512 \times 512$
encoder1	2× conv→ReLU	$64 \times 512 \times 512$
	max-pooling	$64 \times 256 \times 256$
encoder1	repeat 3×	$512 \times 32 \times 32$
	Dropout with $p_i = 0.5$	$512 \times 32 \times 32$
center	2× conv→ReLU	$1024 \times 28 \times 28$
	Dropout with $p_i = 0.5$	$512 \times 28 \times 28$
	up-conv→ReLU	$512 \times 56 \times 56$
decoder1	concat. encoder maps	$1024 \times 56 \times 56$
	2× conv→ReLU	$512 \times 52 \times 52$
	up-conv→ReLU	$256 \times 104 \times 104$
decoder1	repeat 3× (no last up-conv)	$64 \times 388 \times 388$
final	conv	$C \times 388 \times 388$
	bilinear upsample	$C \times 512 \times 512$

Table 1 Our implementation of UNet’s network architecture [25]. Unlike the original authors, we have added a padding of 1 and a final upsampling layer to the encoder to obtain matching input and output dimensions.

In addition, the stored encoder feature maps are concatenated after upsampling and fed into the convolution of the decoder. Finally, a 1×1 convolution creates the final segmentation output. UNet has a large number of feature maps and therefore the largest number of learnable parameters of the networks investigated in this study (see Tab. 8). UNet’s architecture is summarized in Tab. 1.

2.3 SegNet

SegNet is an efficient, deep, fully convolutional neural network with a symmetrical encoder and decoder architecture [3]. Each encoder layer in the network performs 3×3 convolutions to create a set of feature maps. After batch normalization (BN), the feature maps are max-pooled to downsample. The indices of the max-pooling layer are saved for later upsampling. This is done to capture and store

Name	Type	Output Size
input	RGB image	$3 \times 512 \times 512$
encoder1	$2 \times \text{conv} \rightarrow \text{BN} \rightarrow \text{ReLU}$	$64 \times 512 \times 512$
	max-pooling	$64 \times 256 \times 256$
encoder1	<i>repeat</i>	$128 \times 128 \times 128$
encoder2	$3 \times \text{conv} \rightarrow \text{BN} \rightarrow \text{ReLU}$	$256 \times 128 \times 128$
	max-pooling	$256 \times 64 \times 64$
encoder2	<i>repeat</i> $2 \times$	$512 \times 16 \times 16$
decoder2	$3 \times \text{conv} \rightarrow \text{BN} \rightarrow \text{ReLU}$	$512 \times 16 \times 16$
	max-unpool	$512 \times 32 \times 32$
decoder2	<i>repeat</i> $2 \times$	$128 \times 128 \times 128$
decoder1	$2 \times \text{conv} \rightarrow \text{BN} \rightarrow \text{ReLU}$	$64 \times 128 \times 128$
	max-unpool	$64 \times 256 \times 256$
decoder1	<i>repeat</i> (without last BN)	$64 \times 512 \times 512$
final	softmax	$C \times 512 \times 512$

Table 2 SegNet’s network architecture [3].

Name	Type	Output Size
input	RGB image	$3 \times 512 \times 512$
initial		$16 \times 256 \times 256$
bottleneck1	downsampling	$64 \times 128 \times 128$
bottleneck1	<i>repeat</i> $4 \times$	$64 \times 128 \times 128$
bottleneck2	downsampling	$128 \times 64 \times 64$
bottleneck2	<i>repeat</i> $8 \times$	$128 \times 64 \times 64$
bottleneck3	<i>repeat</i> $8 \times$	$128 \times 64 \times 64$
bottleneck4	upsampling	$64 \times 128 \times 128$
bottleneck4	<i>repeat</i> $2 \times$	$64 \times 128 \times 128$
bottleneck5	upsampling	$16 \times 256 \times 256$
bottleneck5	<i>repeat</i>	$16 \times 256 \times 256$
final	up-conv	$C \times 512 \times 512$

Table 3 Our implementation of the network architecture of ENet [20].

the boundary information of the objects that would otherwise be lost after down-sampling. On the other side, the corresponding decoder first upsamples its input by using the saved max-pooling indices from encoding (max-unpooling). Next, the resulting feature maps are convolved again. A final softmax classifier outputs a C channel image of class probabilities. In contrast to UNet, transferring only max-pooling indices reduces memory consumption. As SegNet’s encoder is identical to the VGG16 [29] network’s convolutional layers, which can be trained on very large image classification datasets, its weights can be used to fine-tune SegNet and therefore improve a segmentation task for smaller datasets. In this study however, we will not use pre-trained weights in order to compare the investigated networks fairly. SegNet’s architecture is summarized in Tab. 2. For later stochastic inference, we added a dropout layer with $p_i = 0.5$ after every pooling/upsampling layer in encoder2 and decoder2 stages. The resulting architecture is also referred to as Bayesian SegNet [13].

2.4 ENet

Efficient Neural Network (ENet) is an architecture with a reduced number of parameters, especially created for low latency tasks in mobile or embedded devices

Name	Type	Output Size
input	RGB image	$3 \times 512 \times 512$
encoder1	2× downsampling	$64 \times 128 \times 128$
	5× non-bt-1D	$64 \times 128 \times 128$
encoder2	downsampling	$128 \times 64 \times 64$
	8× non-bt-1D	$128 \times 64 \times 64$
decoder2	up-conv	$64 \times 128 \times 128$
	2× non-bt-1D	$64 \times 128 \times 128$
decoder1	up-conv	$16 \times 256 \times 256$
	2× non-bt-1D	$16 \times 256 \times 256$
final	up-conv	$C \times 512 \times 512$

Table 4 Network architecture of ErfNet [24].

[20]. In contrast to SegNet, it has an asymmetric structure with a large encoder and a small decoder. The network consists of a repeating basic module, which first splits its input into two branches. The main branch performs three convolutions with batch normalization and a final spatial dropout with $p_i = 0.01$ in the first stage and $p_i = 0.1$ afterwards. The outer 1×1 convolutions reduce and increase the number of feature maps respectively, forming a “bottleneck” around the inner convolution. The side branch just copies or copies and downsamples (max-pools) the input, which acts as a shortcut to the main branch. As in SegNet, the max-pooling indices are saved for later upsampling by max-unpooling. In the end, both branches are reunited by element-wise addition with PReLU activation. The final stage is a transposed convolution to generate a C channel image with input resolution. In the very beginning, a two-branched initial stage of convolution and max-pooling, which are merged by concatenation, is applied. With this architecture, ENet has the lowest number of trainable parameters in this study (see Tab. 3 and Tab. 8).

2.5 ErfNet

ErfNet stands for “Efficient Residual Factorized Network” and tries to provide a compromise between accuracy and efficiency [24]. It is composed of layers, which are similar to the bottleneck modules, but instead the 2D convolutions are factorised into 1D convolutions. The resulting layers are called non-bottleneck-1D (non-bt-1D) and drastically reduce computational cost and the number of parameters. The network architecture is summarized in Tab. 4 and forms an encoder-decoder structure similar to ENet. The downsampling modules are the same as the initial module of ENet. Dropout is included in all non-bt-1D layers with $p_i = 0.3$ in the last stage and $p_i = 0.03$ before of that. Instead of max-unpooling, the upsampling block contains transposed convolution.

2.6 Evaluation Setup

In order to evaluate the previously described segmentation methods, performance is assessed on our in vivo vocal fold dataset. At first, all models are implemented in Python using the PyTorch [21] library with CUDA backend. To train the models, we split the dataset as follows. SEQ1 and SEQ8 are used as training set (218 images), the first half of SEQ7 is used as validation set (61 images), and SEQ2,

SEQ3, and the second half of SEQ7 are used as test set (121 images). We train the models on the training set and evaluate the inter-training accuracy on the validation set. The test set is left out for final performance assessment. As accuracy metric, we use the popularly accepted Intersection-over-Union (IoU) metric:

$$\text{IoU} = \frac{\text{TP}}{\text{TP} + \text{FP} + \text{FN}} \quad (1)$$

with the number of true positive (TP), false positive (FP) and false negative (FN) pixels. The IoU metric is calculated for each of the 7 classes independently.

All models are trained in an end-to-end manner using the ADADELTA [33] stochastic gradient descent optimizer with an adaptive per-dimension learning rate, a weight decay of $1 \cdot 10^{-4}$ and a batch size of 6. The advantage of ADADELTA is that there is no need for choosing an initial learning rate or learn rate decay. Therefore, no further tuning of the learning rate is applied. For later evaluation, we choose the best-performing weight configuration after training for at least 500 epochs on a single GPGPU (GeForce GTX 1080 Ti, Nvidia Corp., Santa Clara, CA, USA). The training objective is to minimize a loss function, which acts as a dissimilarity measure between a prediction of the model $\hat{\mathbf{y}}$ and the corresponding ground truth label map \mathbf{y} . The prediction $\hat{\mathbf{y}}$ is a tensor and expected to have the shape $\mathbb{R}^{C \times H \times W}$ with the height H , width W , and number of classes C of the input image. For every pixel of the input image, we get a probability distribution containing the estimated class probabilities. In order to match the output dimensions of the models, we employ one-hot encoding scheme where a ground truth label map \mathbf{y} is reshaped to $\mathbb{R}^{C \times H \times W}$. After that, the ground truth distribution for each pixel contains only one entry with 1 and otherwise 0, assigning a unique class to each pixel.

As loss function, we choose a weighted negative log-likelihood (or cross entropy) function which is defined for a distribution $\mathbf{p} = \hat{\mathbf{y}}_{h,w}$ of a single pixel of true class c as

$$l(\mathbf{p}, c) = -\mathbf{w}_c \log \left(\frac{\exp(\mathbf{p}_c)}{\sum_{j=0}^{C-1} \exp(\mathbf{p}_j)} \right) \quad (2)$$

with weight vector

$$\mathbf{w}_c = \frac{\sum_{j=0}^{C-1} N(j)}{C \cdot N(c)} \in \mathbb{R}^C, \quad (3)$$

where $N(c)$ is the total number of occurrences of pixels with class c in the whole dataset. Vector \mathbf{w} contains a weight for each class. This is done to give less occurring classes, such as “pathology”, more weight when calculating the loss. Otherwise, omitting classes with small areas would result in a relatively small overall error. For one prediction $\hat{\mathbf{y}}$ the total loss becomes

$$L(\hat{\mathbf{y}}, \mathbf{y}) = \sum_{h=0}^{H-1} \sum_{w=0}^{W-1} l(\hat{\mathbf{y}}_{h,w}, \mathbf{y}_{h,w}) . \quad (4)$$

2.7 Model Uncertainty

In safety-critical tasks, such as medical imaging, it is important to know the confidence of the prediction of a model, especially when using the information for

(semi-)autonomous robot or laser control. According to [10], the class probabilities produced by a softmax function approximate relative probabilities between class labels and give no overall measure of the model’s uncertainty. Therefore, we also evaluate each prediction uncertainty by Monte Carlo sampling with dropout at test time, following the framework of [13] (also called *stochastic inference*). This gives us an approximation of the distribution of the softmax class probabilities for every pixel of the model prediction. We are using the *variance* $\sigma_{c,h,w}^2$ of each softmax probability as a per-class uncertainty and the *mean of the variances* $\bar{\sigma}_{h,w}^2$ with respect to c as an overall uncertainty. During Monte Carlo sampling we set the dropout probabilities to be the same as during training.

3 Results

In the following, we present the results of the four different segmentation methods from the aforementioned evaluation setup. Table 5, 6, and 7 summarize the results by showing the per-class and mean segmentation accuracy on the test set measured with the Intersection-over-Union metric. The highest mean IoU value on SEQ2 and SEQ3 is achieved by ErfNet, which has also the highest per-class IoU for the classes *vocal folds* and *other tissue* on both sequences. ErfNet has also scored best results in the overall poorly segmented class *pathology*. The advantage of ErfNet is smaller on SEQ3 and it is outperformed by ENet and SegNet on the classes *surgical tool* and *intubation*. On SEQ7.2, ENet obtains the best result regarding mean IoU. With a mean IoU of 59.2% ErfNet is slightly worse, but can achieve better results than ENet for classes *other tissue* and *intubation*. UNet provides the worst mean results on all test sequences.

In general, the class *pathology* is the worst recognized. It was de facto not recognized by SegNet and ENet. This can be explained by the fact that this class has a significantly lower occurrence in the whole dataset (see Fig. 2), even lower than *void*, which has not been considered for accuracy assessment. The second worst class IoU was achieved for *other tissue* on SEQ3. By looking at the qualitative results in Fig. 3, this can be explained by the fact, that one vocal fold has been surgically manipulated and shows bleeding. This was not covered in the training set and the models tend to classify it to *other tissue*. However, good results can be achieved for classes *surgical tool* and *other tissue* on SEQ7.2.

Figure 3 shows class label predictions for selected example images from the test set sequences. As expected from the IoU values, the prediction of UNet has major errors in class *glottal space*, *pathology*, and on the edges between two adjacent areas. The result of SegNet on *glottal space* is better in general, but it provides visible errors in class *vocal folds* and *intubation*. ENet and ErfNet both achieve good results, with ErfNet even resolving parts of *pathology*. When zooming into the label maps, it is visible that ENet has a strong aliasing effect on the edges, whereas ErfNet results in smoother edges.

The prediction uncertainties in Fig. 3 give an estimate on how confident the model is for a specific pixel of the selected images. UNet and SegNet use normal dropout for stochastic inference, whereas ENet and ErfNet use spatial dropout (turning off full feature maps). In contrast to normal dropout, there is currently no proof of spatial dropout acting as Bayesian approximation [10]. This must be taken into account when considering the uncertainty maps. It is worth mentioning that

SEQ2	1	2	3	4	5	6	mean
UNet	51.3	45.8	9.99	7.73	25.6	23.7	27.3
SegNet	29.4	37.6	43.9	0.1	44.6	54.5	35.0
ENet	45.4	42.1	34.3	1.0	40.0	33.7	32.8
ErfNet	71.8	71.9	45.6	16.0	36.4	57.8	49.9
mean	49.5	49.4	33.4	6.2	36.7	42.4	

Table 5 Per-class and mean IoU (%) on SEQ2.

SEQ3	1	2	3	4	5	6	mean
UNet	32.4	14.4	7.64		12.3	27.0	18.8
SegNet	15.8	11.6	32.8		28.4	58.6	29.4
ENet	38.5	14.5	25.5		28.7	32.6	28.0
ErfNet	63.2	25.4	26.1		23.3	45.7	36.7
mean	37.5	16.5	23.0		23.2	41.0	

Table 6 Per-class and mean IoU (%) on SEQ3. Class 4 (*pathology*) was not present in this sequence.

SEQ7.2	1	2	3	4	5	6	mean
UNet	48.3	51.4	17.1		90.9	56.1	52.8
SegNet	51.3	58.7	33.2		91.9	51.6	57.3
ENet	40.0	58.6	48.7		92.4	62.6	60.5
ErfNet	48.6	60.0	31.5		92.3	63.8	59.2
mean	47.1	57.2	32.6		91.9	58.5	

Table 7 Per-class and mean IoU (%) on second half of SEQ7. Class 4 (*pathology*) was not present in this sequence.

ENet and ErfNet have a higher uncertainty in general and especially on *surgical tool* and *intubation*. A possible explanation for this could be the low numbers of parameters having less redundancies compared to UNet and SegNet (see Tab. 8). This has to be investigated in future work. Furthermore, it can be observed that ENet and ErfNet show a high uncertainty around the location where *pathology* should be. On the other hand, both show low uncertainties on *vocal folds* on all of the three test sequences. This can be interpreted as good generalization for this class.

Figure 4 shows the recorded mean loss during training on both the training and validation sets. All models converge in our training setup with ENet and ErfNet converging significantly faster. The later upward trend of the validation loss of UNet indicates overfitting of the training set. However, short-term overfitting can also be observed on ENet and ErfNet. As soon as the training loss gets close to $\bar{L} = 0$, the validation loss increases.

Table 8 shows the mean inference times including memory transfer to the GPGPU. All models are able to process the images fairly efficiently with at least 20 frames per second (fps). ENet and ErfNet, however, perform significantly better, with ENet achieving the best performance (108.5 fps).

4 Conclusion and outlook

In this paper, a novel dataset of laryngeal surgery images with ground truth segmentation maps has been introduced. The dataset is used for a comparative study

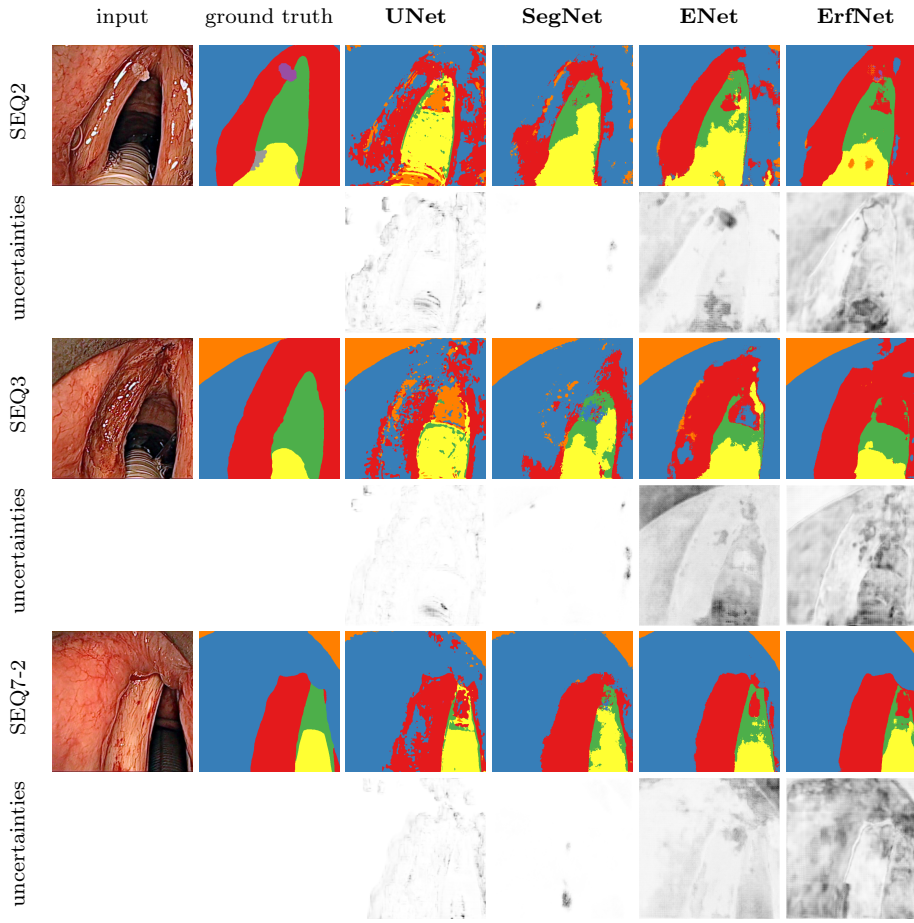


Fig. 3 Qualitative results of the different models on exemplary images of the test set sequences and corresponding prediction uncertainties of all classes (gray level denotes variance with white where $\bar{\sigma}_{h,w}^2 = 0$).

Network	trainable parameter	512×512	
		ms	fps
UNet	31,032,200	47.2	21.18
SegNet	29,447,624	45.7	21.9
ENet	392,420	9.22	108.5
ErfNet	2,064,508	11.1	90.1

Table 8 Total number of trainable parameters and mean inference times on a single GeForce GTX 1080 Ti (including data to GPGPU transfer).

of recent CNN-based segmentation methods. It has been shown that of the methods investigated, ENet and ErfNet yielded the most successful results on segmenting endoscopic image data with high efficiency. Schoob et al. [26] reported that image-based online control of incision lasers for soft tissue undergoing motion is feasible with an imaging pipeline running at 73.5 Hz. Therefore, both ENet and ErfNet are

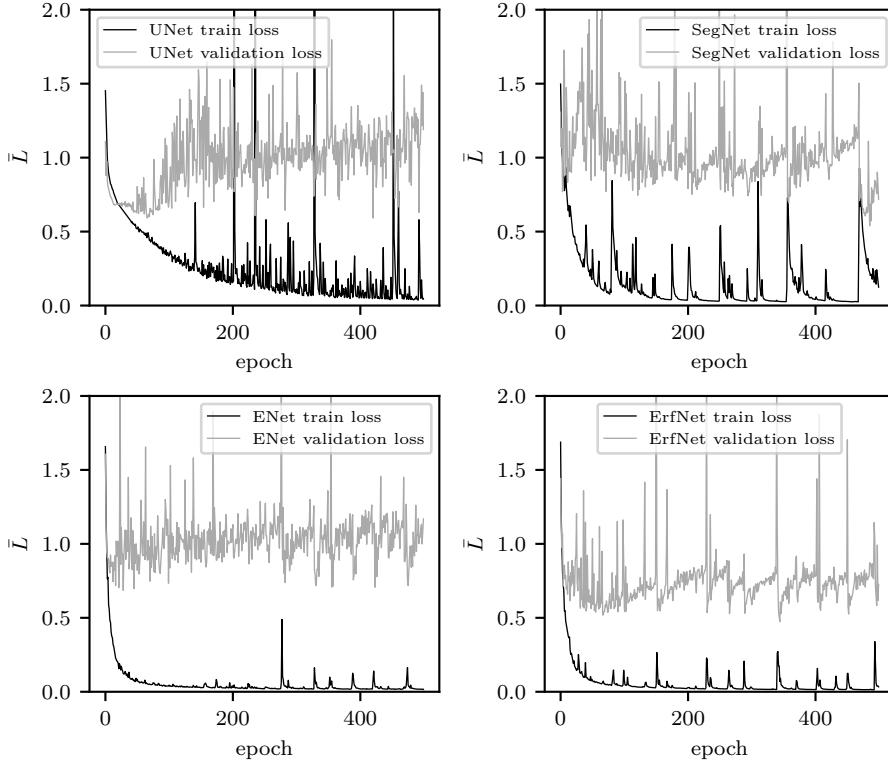


Fig. 4 Mean losses during training for 500 epochs.

well-suited in terms of efficiency for later use for laser control in a medical imaging device. The reported laser incision error of their approach was 0.12–0.21 mm. With monoscopic images, we cannot directly compare our segmentation accuracy to this and would like to address this in future work. The raw data, from which our dataset images are chosen, consist of stereo images. Currently, the dataset only includes the left images. By segmenting both the left and the right stereo images, a metric accuracy value for the segmentation task can be stated, if calibration data is available.

When comparing UNet and SegNet to ENet and ErfNet, two main characteristics differ. The first difference is that the first two have a symmetrical auto-encoder structure, while the latter two have a significantly smaller decoder. It is assumed that a higher performance can be attributed to the encoder, while the decoder only upsamples the output of the encoder [20]. The second difference is long-term connections between encoder and decoder layers, bypassing the deeper structures, by copying whole feature maps in UNet or by memorizing the pooling indices in SegNet. However, ENet and ErfNet do not have such connections. The bottleneck units bypass only one layer.

It has been shown that in medical image analysis, fine-tuning of a pre-trained CNN outperforms training from scratch [30]. In future work, we would like to pre-train on large, publicly available segmentation datasets, such as Cityscapes [7],

to increase the segmentation accuracy. In addition, an extension of the dataset to different pathologies can enable automated diagnosis. Further improvement regarding our dataset and the generation of ground truth information for medical imaging is required.

The major drawback of our dataset is the low number of images and the unbalanced class occurrences. The most important class *pathology* is the least occurring. Not every sequence contains every class. This also explains the unsatisfying results on SEQ3. Ongoing work will therefore focus on enlarging the dataset by investigating self-supervised segmentation methods, where a human expert accepts or discards the segmentation prediction. Beyond that, improvements can be achieved by modelling the uncertainty, especially for small datasets like ours [13], and by combining CNN-based segmentation with tracking [11]. Future work will focus on comprehensive evaluation under clinical conditions. A later goal is the combination of these algorithms with the control of robots and lasers for automation in surgery.

Acknowledgements We thank Giorgio Peretti from the Ospedale Policlinico San Martino, University of Genova, Italy, for providing us with the in vivo laryngeal data used in this study. We would also like to thank James Napier from the Institute of Lasers and Optics, University of Applied Sciences Emden-Leer, Germany, for his thorough proofreading of this manuscript.

Disclosure of potential conflicts of Interest

Conflict of Interest The authors declare that they have no conflict of interest.

Funding This research has received funding from the European Union as being part of the ERFE OPhonLas project.

Formal Consent The endoscopic video images were acquired by Prof. Giorgio Peretti (Director of Otorhinolaryngology at Ospedale Policlinico San Martino, University of Genova). Patients gave their written consent for the procedure and the use of the data. No further approval is necessary for such endoscopic recordings. The videos were anonymized made available inside the μ RALP consortium for further usage. All procedures performed in studies involving human participants were in accordance with the ethical standards of the institutional and/or national research committee and with the 1964 Helsinki declaration and its later amendments or comparable ethical standards.

References

1. Allin, S., Galeotti, J., Stetten, G., Dailey, S.H.: Enhanced snake based segmentation of vocal folds. In: IEEE International Symposium on Biomedical Imaging: Nano to Macro, vol. 1, pp. 812–815 (2004)
2. Aubreville, M., Knipfer, C., Oetter, N., Jaremenko, C., Rodner, E., Denzler, J., Bohr, C., Neumann, H., Stelzle, F., Maier, A.: Automatic Classification of Cancerous Tissue in Laserendomicroscopy Images of the Oral Cavity using Deep Learning. *Scientific Reports* **7**(1) (2017). DOI 10.1038/s41598-017-12320-8
3. Badrinarayanan, V., Kendall, A., Cipolla, R.: Segnet: A deep convolutional encoder-decoder architecture for image segmentation. *IEEE Transactions on Pattern Analysis and Machine Intelligence* (2017)

4. Barbalata, C., Mattos, L.S.: Laryngeal Tumor Detection and Classification in Endoscopic Video. *IEEE Journal of Biomedical and Health Informatics* **20**(1), 322–332 (2016). DOI 10.1109/JBHI.2014.2374975
5. Barkmeier-Kraemer, J.M., Patel, R.R.: The next 10 years in voice evaluation and treatment. *Semin Speech Lang* **37**(03), 158–165 (2016). DOI 10.1055/s-0036-1583547
6. Cabezas, M., Oliver, A., Lladó, X., Freixenet, J., Cuadra, M.B.: A review of atlas-based segmentation for magnetic resonance brain images. *Computer Methods and Programs in Biomedicine* **104**(3), e158–e177 (2011). DOI 10.1016/j.cmpb.2011.07.015
7. Cordts, M., Omran, M., Ramos, S., Rehfeld, T., Enzweiler, M., Benenson, R., Franke, U., Roth, S., Schiele, B.: The cityscapes dataset for semantic urban scene understanding. In: *Proc. of the IEEE Conference on Computer Vision and Pattern Recognition (CVPR)* (2016)
8. Doignon, C., Graebbling, P., de Mathelin, M.: Real-time segmentation of surgical instruments inside the abdominal cavity using a joint hue saturation color feature. *Real-Time Imaging* **11**(5), 429–442 (2005). DOI 10.1016/j.rti.2005.06.008
9. Friedrich, D.T., Scheithauer, M.O., Greve, J., Duvvuri, U., Sommer, F., Hoffmann, T.K., Schuler, P.J.: Potential Advantages of a Single-Port, Operator-Controlled Flexible Endoscope System for Transoral Surgery of the Larynx. *Annals of Otolaryngology, Rhinology & Laryngology* **124**(8), 655–662 (2015). DOI 10.1177/0003489415575548
10. Gal, Y., Ghahramani, Z.: Dropout as a Bayesian Approximation: Representing Model Uncertainty in Deep Learning. *Proc. 33rd Int. Conf. Mach. Learn.* **48** (2016)
11. García-Peraza-Herrera, L.C., Li, W., Gruijthuisen, C., Devreker, A., Attilakos, G., Deprest, J., Poorten, E.V., Stoyanov, D., Vercauteren, T., Ourselin, S.: Real-time segmentation of non-rigid surgical tools based on deep learning and tracking. *Lect. Notes Comput. Sci.* **10170 LNCS**, 84–95 (2017). DOI 10.1007/978-3-319-54057-3_8
12. He, K., Zhang, X., Ren, S., Sun, J.: Delving Deep into Rectifiers: Surpassing Human-Level Performance on ImageNet Classification. In: *IEEE Int. Conf. Comput. Vis.*, pp. 1026–1034 (2015). DOI 10.1109/ICCV.2015.123
13. Kendall, A., Badrinarayanan, V., Cipolla, R.: Bayesian segnet: Model uncertainty in deep convolutional encoder-decoder architectures for scene understanding. *arXiv preprint arXiv:1511.02680* (2015)
14. Long, J., Shelhamer, E., Darrell, T.: Fully convolutional networks for semantic segmentation. In: *Proc. IEEE Comput. Soc. Conf. Comput. Vis. Pattern Recognit.*, pp. 3431–3440 (2015). DOI 10.1109/CVPR.2015.7298965
15. Noble, J.A., Boukerroui, D.: Ultrasound image segmentation: a survey. *IEEE Transactions on Medical Imaging* **25**(8), 987–1010 (2006). DOI 10.1109/TMI.2006.877092
16. Olabarriaga, S.D., Smeulders, A.W.M.: Interaction in the segmentation of medical images. *Medical Image Analysis* **5**, 127–142 (2001)
17. Osma-Ruiz, V., Godino-Llorente, J.I., Sáenz-Lechón, N., Fraile, R.: Segmentation of the glottal space from laryngeal images using the watershed transform. *Computerized Medical Imaging and Graphics* **32**(3), 193–201 (2008). DOI j.compmedimag.2007.12.003
18. Pal, N.R., Pal, S.K.: A review on image segmentation techniques. *Pattern Recognition* **26**(9), 1277–1294 (1993). DOI 10.1016/0031-3203(93)90135-J
19. Panek, D., Skalski, A., Zielinski, T., Deliyski, D.D.: Voice pathology classification based on High-Speed Videoendoscopy. In: *Annual International Conference of the IEEE Engineering in Medicine and Biology Society (EMBC)*, pp. 735–738 (2015). DOI 10.1109/EMBC.2015.7318467
20. Paszke, A., Chaurasia, A., Kim, S., Culurciello, E.: ENet: A Deep Neural Network Architecture for Real-Time Semantic Segmentation. *ArXiv e-prints* (2016). URL <http://arxiv.org/abs/1606.02147>
21. Paszke, A., Gross, S., Chintala, S., Chanan, G., Yang, E., DeVito, Z., Lin, Z., Desmaison, A., Antiga, L., Lerer, A.: Automatic differentiation in PyTorch. In: *31st Conference on Neural Information Processing Systems (NIPS)* (2017). URL <https://openreview.net/forum?id=BJJsrnfcZ>
22. Phung, S.L., Bouzerdoum, A., Chai, D.: Skin segmentation using color pixel classification: analysis and comparison. *IEEE Transactions on Pattern Analysis and Machine Intelligence* **27**(1), 148–154 (2005). DOI 10.1109/TPAMI.2005.17
23. Rajab, M., Woolfson, M., Morgan, S.: Application of region-based segmentation and neural network edge detection to skin lesions. *Computerized Medical Imaging and Graphics* **28**(1), 61–68 (2004). DOI 10.1016/S0895-6111(03)00054-5

24. Romera, E., Álvarez, J.M., Bergasa, L.M., Arroyo, R.: ERFNet : Efficient Residual Factorized ConvNet for Real-time Semantic Segmentation. *IEEE Trans. Intelligent Transp. Syst.* **19**(1), TBD (2018). DOI 10.1109/TITS.2017.2750080
25. Ronneberger, O., Fischer, P., Brox, T.: U-Net: Convolutional Networks for Biomedical Image Segmentation pp. 1–8 (2015). DOI 10.1007/978-3-319-24574-4_28. URL <http://arxiv.org/abs/1505.04597>
26. Schoob, A., Kundrat, D., Kahrs, L.A., Ortmaier, T.: Stereo vision-based tracking of soft tissue motion with application to online ablation control in laser microsurgery. *Medical Image Analysis* **40**, 80–95 (2017). DOI <https://doi.org/10.1016/j.media.2017.06.004>
27. Schoob, A., Kundrat, D., Lekon, S., Kahrs, L.A., Ortmaier, T.: Color-encoded distance for interactive focus positioning in laser microsurgery. *Optics and Lasers in Engineering* **83**, 71–79 (2016). DOI <https://doi.org/10.1016/j.optlaseng.2016.03.002>
28. Schoob, A., Laves, M.H., Kahrs, L.A., Ortmaier, T.: Soft tissue motion tracking with application to tablet-based incision planning in laser surgery. *Int. J. Comput. Assist. Radiol. Surg.* (2016). DOI 10.1007/s11548-016-1420-5
29. Simonyan, K., Zisserman, A.: Very deep convolutional networks for large-scale image recognition. *ArXiv e-prints* (2014). URL <https://arxiv.org/abs/1409.1556>
30. Tajbakhsh, N., Shin, J.Y., Gurudu, S.R., Hurst, R.T., Kendall, C.B., Gotway, M.B., Liang, J.: Convolutional neural networks for medical image analysis: Full training or fine tuning? *IEEE Transactions on Medical Imaging* **35**(5), 1299–1312 (2016). DOI 10.1109/TMI.2016.2535302
31. Turkmen, H.I., Karsligil, M.E., Kocak, I.: Classification of laryngeal disorders based on shape and vascular defects of vocal folds. *Computers in Biology and Medicine* **62**, 76–85 (2015). DOI <https://doi.org/10.1016/j.combiomed.2015.02.001>
32. Unger, J., Lohscheller, J., Reiter, M., Eder, K., Betz, C.S., Schuster, M.: A Noninvasive Procedure for Early-Stage Discrimination of Malignant and Precancerous Vocal Fold Lesions Based on Laryngeal Dynamics Analysis. *Cancer Research* **75**(1), 31–39 (2015). DOI 10.1158/0008-5472.CAN-14-1458
33. Zeiler, M.D.: ADADELTA: An Adaptive Learning Rate Method. *ArXiv e-prints* (2012). URL <https://arxiv.org/abs/1212.5701>